New Splitting Algorithms for Geometric Transformations of Digital Images and Their Error Analysis

Zi-Cai Li,[1,2] John Y. Chiang,[2] C. Y. Suen[3]

[1] Department of Applied Mathematics, National Sun Yat-sen University, Kaohsiung, Taiwan

[2] Department of Computer Science and Engineering, National Sun Yat-sen University, Kaohsiung, Taiwan

[3] Centre for Pattern Recognition and Machine Intelligence, Concordia University, 1455 de Maissonneuve Blvd. West, Montreal, Quebec H3G 1M8, Canada

Received 18 August 2011; accepted 29 September 2011

ABSTRACT: For digital images and patterns under the nonlinear geometric transformation, T: $(\xi, \eta) \to (x, y)$, this study develops the splitting algorithms (i.e., the pixel-division algorithms) that divide a 2D pixel into $N \times N$ subpixels, where N is a positive integer chosen as $N = 2^k (k \geq 0)$ in practical computations. When the true intensity values of pixels are known, this method makes it easy to compute the true intensity errors. As true intensity values are often unknown, the proposed approaches can compute the sequential intensity errors based on the differences between the two approximate intensity values at N and $N/2$. This article proposes the new splitting–shooting method, new splitting integrating method, and their combination. These methods approximate results show that the true errors of pixel intensity are $O(H)$, where H is the pixel size. Note that the algorithms in this article do not produce any sequential errors as $N \geq N_0$, where N_0 (≥ 2) is an integer independent of N and H. This is a distinctive feature compared to our previous papers on this subject. The other distinct feature of this article is that the true error bound $O(H)$ is well suited to images with all kinds of discontinuous intensity, including scattered pixels. Int J Imaging Syst Technol, 21, 323–335, 2011; Published online in Wiley Online Library (wileyonlinelibrary.com). DOI 10.1002/ima.20298

Key words: image geometric transformation; digital images; splitting algorithms; splitting–shooting method; error analysis

I. INTRODUCTION

Digital images and patterns often undergo changes and distortions due to linear or nonlinear transformations. Common examples of such images include handwritten characters, photos, and human faces in different orientations and different appearances. Consider the 2D nonlinear transformation

$$T : (\xi, \eta) \to (x, y), \quad x = x(\xi, \eta), \quad y = y(\xi, \eta), \tag{1}$$

where (x, y) and (ξ, η) are the coordinates of points in XOY and $\xi O \eta$, respectively, and XOY and $\xi O \eta$ are two Cartesian coordinate systems. First, assume that the functions $x(\xi, \eta)$ and $y(\xi, \eta)$ are explicit and known. A cycle conversion $T^{-1}T$ of image transformations occurs if a transformation T distorts an image, and then restores back to itself by the inverse transformation T^{-1}. This article also studies the cyclic conversion $T^{-1}T$ for digital images because the original intensity values of pixels remain exactly the same after this conversion. The true intensity errors of restoration can be computed for the algorithms used. The cyclic transformation $T^{-1}T$ represents the restoration of distorted images, which is important in pattern recognition.

Splitting algorithms divide a 2D pixel into $N \times N$ subpixels, where N is a positive integer $N = 2^k (k \geq 0)$ in practical computation. When the true intensity values of pixels are known, the true intensity errors can be easily computed. As the true intensity values are often unknown, the sequential intensity errors may be computed using the differences between the two approximate intensity values at N and $N/2$. The strict definitions of sequential intensity errors are given in (58) and (61) later.

Previous research (Li, 1990) proposed the area method to carry out linear transformations using exact integration. However, for nonlinear transformations, splitting a pixel into N^2 subpixels produces approximate integration and results in sequential errors of $O(1/N^p)$ with the power $p \geq 1$. The remarkable advantage of the original combination CSIM of splitting–shooting–integration methods is the omission of nonlinear solutions, if the explicit functions of the forward transformations T are known. The sequential errors are proven to be of $O(1/N)$ by Li (1996) and $O_p(1/N^{1.5})$ in probability of Li and Bai (1998). As the initial sequential errors of CSIM are large, the number N is also large for a system with multiple (e.g., 256) levels of intensity. Therefore, CSIM is limited to binary images (Li et al., 1989) and small number of pixels. This article develops new algorithms that are suitable for a huge number of pixels with 256 intensity levels.

For arbitrary nonlinear transformations, it is desirable to avoid nonlinear solutions in the algorithms due to two difficulties: (1) the existence and uniqueness of the solutions and (2) good initial values for the iteration methods, such as the Newton iteration method. A

Correspondence to: John Y. Chiang; e-mail: chiang@cse.nsysu.edu.tw

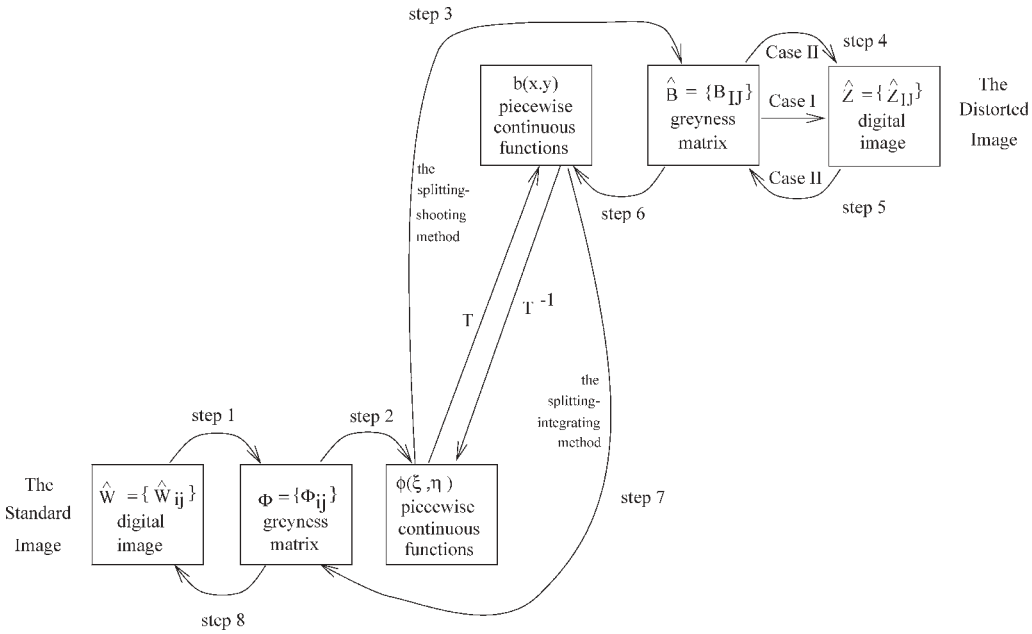

Figure 1. Schematic steps in digital image transformations by numerical approaches.

recent study discusses approximate nonlinear transformations through piecewise linear transformations. This is more significant for complicated transformations in which the transformation functions are not explicitly given, but governed by partial differential equations (PDEs) of Li, (1996) and Li et al. (1989). The finite element method with piecewise linear intensity functions may approximate these PDEs. A new approach of approximating $_T$ as piecewise linear transformations makes it possible to bypass nonlinear solutions. The other important aspect of the proposed approach is that it gets rid of sequential intensity errors by NCSIM, if the pixel is split into $N \times N$ subpixels, where the integer $N \geq N_0 \geq 2$, and N_0 is independent of N and H. Our previous study (Li, 1989, 1990, 1994, 1996, 1999, 1998, 2001, 2004) developed different numerical algorithms that always generate sequential errors.

The first goal of this article is to develop new algorithms that avoid sequential errors when N exceeds $N0$. Hence, this approach may choose a smaller division number $N \geq N_0$, thus to greatly save the central processing unit (CPU) time and computer storage. More importantly, the new algorithms are applicable to a huge number of pixels with 256 intensity levels. The second goal of this article is to explore the new error analysis in Section IV. This method is applicable to the images with all kinds of discontinuous intensity, including scattered pixels in real-life application. This is remarkably different from our previous analysis (Li, 1989, 1990, 1994, 1996, 1999, 1998, 2001, 2004), where the smooth intensity of images is always assumed unrealistically.

Although interpolation can be used for large jumps of intensity function, their true errors are, of course, large. However, the sequential errors will diminish for $N \geq N_0$. This article also derives the true errors as $O(H)$, where H is the pixel size.

This article is organized as follows. Section II describes the basic algorithms, SSM, SIM, and CSIM for T, T^{-1}, and $T^{-1}T$, respectively. Section III adopts piecewise linear interpolations for nonlinear transformations, and develops the new algorithms, new splitting–shooting method (NSSM), new splitting–integrating method (NSIM), and their combination (NCSIM) for T, T^{-1}, and $T^{-1}T$, respectively. Section IV presents the new error analysis method that may be applied to discontinuity of intensity of images. Section V carries out numerical experiments to confirm the error analysis, and applies numerical algorithms to the geometric transformations governed by PDEs. Finally, the last section provides a few concluding remarks.

II. BASIC SPLITTING ALGORITHMS

This section describes the basic algorithms, SSM; SIM and CSIM.

A. Basic Approach. Let $\hat{W}$ and $\hat{Z}$ denote the original image and the image distorted by geometric transformations, respectively. $\hat{W}$ and $\hat{Z}$ consist of pixels $\hat{W}_{ij}$ and $\hat{Z}_{IJ}$, denoted by $\hat{W} = \{\hat{W}_{ij}\}$ and $\hat{Z} = \{\hat{Z}_{IJ}\}$, respectively. Hence, an image undergoing cyclic conversion can be expressed as

$$\hat{W} \xrightarrow{T} \hat{Z} \xrightarrow{T^{-1}}, \quad \hat{W} = \{\hat{W}_{ij}\}, \quad \hat{Z} = \{\hat{Z}_{IJ}\}, \tag{2}$$

where the pixels $\hat{W}_{ij}$ and $\hat{Z}_{IJ}$ are located at the points (i, j) and (I, J), respectively,

$$(i,j) = \{(\xi, \eta) | \xi = iH, \eta = jH\}, \quad (I,J) = \{(x,y) | x = IH, y = JH\}, \tag{3}$$

and H is the pixel size. Note that for the one-to-one correspondence transformation T, the normalized image $\hat{W}$ under $T^{-1}T$ is exactly the same as the original image $\hat{W}$. Therefore, the proposed approach applies numerical methods to perform (2), as the eight steps illustrated in Figure 1.

Steps 1 and 8 convert image pixels to their intensity values, and vice versa. Denote the intensity values Φ_{ij} and B_{IJ} for the pixels $\hat{W}_{ij}$ and $\hat{Z}_{IJ}$, respectively, and $\hat{W}_{ij}$ (or $\hat{Z}_{IJ}$) for pixels at the positions (i, j) (or (I, J)) with the kth level of a multiple level system of intensity, where Φ_{ij} (or B_{IJ}) are their intensity values with non-negative integers or numbers $\in[0,1]$. Consider the $q(=256)$ level system of intensity as an example. Step 1 can convert the pixel $\hat{W}_{ij}$ of the original image at the kth level to the intensity values Φ_{ij} using the following formula:

$$\Phi_{ij} = \frac{k-1}{q-1}, \quad 0 \le k \le q. \tag{4}$$

For binary images, the pixel $\hat{W}_{ij}$ is either black, denoted by ''*,'' or white, denoted by ''.'' These pixel values are converted to either $\Phi_{ij} = 1$ or $\Phi_{ij} = 0$. The term Φ_{ij} can be regarded as an entry of the grayness matrix $\hat{\Phi}$, denoted by $\hat{\Phi} = \{\Phi_{ij}\}$. This is the traditional matrix representation of images. Conversely, when Step 8 obtains the intensity value $\tilde{\Phi}_{ij}$, the following formulas identify the pixel $\hat{W}_{ij}$ at the kth level of intensity,

$$\tilde{W}_{ij} = \begin{cases} \text{the first level}, & \text{when } \tilde{\Phi}_{ij} < \frac{1}{2(q-1)}, \\ \text{the } k\text{th level}, & \text{when } \frac{k-1}{q-1} - \frac{1}{2(q-1)} \le \tilde{\Phi}_{ij} < \frac{k-1}{q-1} + \frac{1}{2(q-1)}, \\ \text{the } q\text{th level}, & \text{when } \tilde{\Phi}_{ij} \ge 1 - \frac{1}{2(q-1)}. \end{cases} \tag{5}$$

B. Interpolation. Step 2 chooses the following piecewise constant and bilinear interpolatory functions.

1. Piecewise constant interpolation ($\mu = 0$)

$$\hat{\phi}_0(\xi, \eta) = \Phi_{ij} \quad \text{in } \square_{ij} \tag{6}$$

where

$$\square_{ij} = \left\{ \begin{matrix} (\xi,\eta), (i-\frac{1}{2})H \le \xi < (i+\frac{1}{2})H, \\ (j-\frac{1}{2})H \le \eta < (j+\frac{1}{2})H \end{matrix} \right\}, \tag{7}$$

and the total domain Ω of the standard image $\hat{W}$ in $\xi O \eta$ is $\Omega = \bigcup_{ij} \square_{ij}$. In (6) and (8), $\hat{\phi}_\mu(\xi, \eta)$ denotes the interpolant of the intensity function based on Φ_{ij}, where μ represents the order of piecewise polynomials.

2. Piecewise bilinear interpolation ($\mu = 1$)

$$\begin{aligned} \hat{\phi}_1(\xi, \eta) = \frac{1}{H^2} [& \Phi_{ij}((i+1)H - \xi)((j+1)H - \eta) \\ & + \Phi_{i+1j}(\xi - iH)((j+1)H - \eta) \\ & + \Phi_{ij+1}((i+1)H - \xi)(\eta - jH) \\ & + \Phi_{i+1j+1}(\xi - iH)(\eta - jH)] \quad \text{in } \bar{\square}_{ij}, \end{aligned} \tag{8}$$

where

$$\bar{\square}_{ij} = \left\{ \begin{matrix} (\xi, \eta), & iH \le \xi \le (i+1)H, \\ & jH \le \eta \le (j+1)H \end{matrix} \right\}, \quad \text{and} \quad \Omega = \bigcup_{ij} \bar{\square}_{ij}. \tag{9}$$

The piecewise constant and linear interpolations with $\mu = 0,1$ can also be regarded as low-order spline interpolations, and piecewise quadratic and cubic interpolations be regarded as spline interpolations with an order of $\mu = 2,3$. These settings are used to design the interpolant functions $\in C^\mu(\Omega)$, which was also studied for image geometric transformation by Li (1994, 2001). When $\mu = 1$, the piecewise linear interpolations and those in Technique I in Section A (subsection of Section III) obtain the continuous function that coincides with the grayness image in terms of pixels. These interpolation techniques can also be used for the big grayness jumps of neighboring pixels (i.e., discontinuity images).

C. Image Presentation by Integrals. A pixel can represent the mean intensity over $\square_{ij}$ (Li et al., 1989), also see Jähne (1997, p. 211), given by

$$\Phi_{ij}^M = \frac{1}{H^2} \iint_{\square_{ij}} \phi(\xi, \eta) d\xi d\eta. \tag{10}$$

Similarly, we have

$$B_{IJ}^M = \frac{1}{H^2} \iint_{\square_{IJ}} b(x, y) dx dy, \tag{11}$$

where

$$\phi(\xi, \eta) = b(x(\xi, \eta), y(\xi, \eta)), \tag{12}$$

and the standard square pixel region

$$\bar{\square}_{IJ} = \left\{ \begin{matrix} (x, y), & (I-\frac{1}{2})H \le x \le (I+\frac{1}{2})H \\ & (J-\frac{1}{2})H \le y \le (J+\frac{1}{2})H \end{matrix} \right\}. \tag{13}$$

According to Gousseau and Morel (2002), it is natural to present images as (continues) first, then their digital counterpart as integral over pixels. When there exists a discontinuity of image intensity, the weak derivatives may be adapted for study. The linkage between natural images and bounded variation is explored study by Gousseau and Morel (2002). The images with intensity discontinuity only at boundary and edges can also be dealt with, based on functions on the Sobolev space $H^1(\Omega)$, where the weak derivatives are square integrable. An analysis of discontinuity images in Sobolev spaces is reported in our other paper. Evidently, the image definitions in (10) and (11) agree with the natural presentation of digital images of Gousseau and Morel (2002). However, these proposed image presentations by integrals easily link discrete images to calculus and numerical analysis (Li, 1989, 1990, 1994, 1996, 1999, 1998, 2001, 2004).

D. Splitting–Shooting Method for Images under *T*. Assume that the Jacobian determinant

$$\vartheta(\xi, \eta) = \begin{vmatrix} \frac{\partial x}{\partial \xi} & \frac{\partial x}{\partial \eta} \\ \frac{\partial y}{\partial \xi} & \frac{\partial y}{\partial \eta} \end{vmatrix} \tag{14}$$

always satisfies

$$0 < \vartheta_0 \le \vartheta(\xi, \eta) \le \vartheta_M, \tag{15}$$

where ϑ_0 and ϑ_M are two bounded constants independent of ξ,η,x, and y, and the constant J_M denotes the maximal value defined by $J_M = \max_\Omega J$. Denote as Ω_{IJ} the transformed region from $\square_{IJ}$ under the inverse transformation T^{-1}. Note that the edges of Ω_{IJ} are generally curves. Reduce integral (11) to

$$B_{IJ} = \frac{1}{H^2} \iint_{\Omega IJ} \phi(\xi, \eta) \vartheta(\xi, \eta) d\xi d\eta, \tag{16}$$

where

$$\square_{IJ} \xrightarrow{T^{-1}} \Omega_{IJ}, \quad \text{i.e.,} \quad \Omega_{IJ} \xrightarrow{T^{-1}} \square_{IJ}. \tag{17}$$

Split the pixel region $\square_{ij}$ in $\xi O\eta$ of $\hat{W}_{ij}$ into $N \times N$ small subregions $\square_{ij,k\ell}$ [or simply called subpixels by Jähne (1997)], that is,

$$\square_{ij} = \bigcup_{k,\ell=1}^{N} \square_{ij,k\ell}, \tag{18}$$

where

$$\square_{ij,k\ell} = \left\{ \begin{array}{ll} (\xi,\eta), & (i-\frac{1}{2})H + (k-1)h \le \xi < (i-\frac{1}{2})H + kh, \\ & (j-\frac{1}{2})H + (\ell-1)h \le \eta < (j-\frac{1}{2})H + \ell h \end{array} \right\}, \tag{19}$$

and h is the boundary length of $\square_{ij,k\ell}$, given by $h = \frac{H}{N}$.

The splitting–shooting method (SSM) sums the contribution of the subpixels $\square_{ij,k\ell}$, whose centroid transformed by T falls into the identifying pixel region $\square_{IJ}$. As a result, we have

$$B_{IJ} = \frac{1}{H^2} \sum_{ij,k\ell} \iint_{\square_{ij,k\ell} \cap \Omega_{IJ}} \phi(\xi,\eta)\vartheta(\xi,\eta)d\xi dy. \tag{20}$$

The following provides the computational algorithms for (20). Denote

$$\square_{ij,k\ell} \xrightarrow{T} \square^*_{ij,k\ell}, \quad \dot{G_{ij,k\ell}} \xrightarrow{T} \dot{G^*_{ij,k\ell}}, \tag{21}$$

where $\dot{G_{ij,kl}}$ is the centroid of $\square_{ij,k\ell}$. Thus

$$\square_{ij,k\ell} \cap \Omega_{IJ} \xrightarrow{T} \square_{ij,k\ell}{}^* \cap \quad \square_{IJ}. \tag{22}$$

This leads to the following approximate integration

$$B_{IJ} \approx \tilde{B}^{(N)}_{IJ} = \left(\frac{h}{H}\right)^2 \sum_{\substack{\forall ij,k\ell \\ \text{satisfying(25)}}} \hat{\phi}_\mu(\dot{G_{ij,k\ell}})\vartheta(\dot{G_{ij,k\ell}}), \quad \mu = 0, 1, \tag{23}$$

where $\hat{\phi}_0$ are $\hat{\phi}_1$ given in (6) and (8), and $\phi(\dot{G}) = \phi(\xi(\dot{G}), \eta(\dot{G}))$. In (23), the notation $\forall ij,k\ell$ satisfying (25) means that the summation is performed for all $\square_{ij,k\ell}$ whose centroid falls into $\square_{IJ}$, denoted by (25). Further, $\tilde{B}^{(N)}_{IJ}$ denotes the approximate intensity values of B_{IJ} with the $N \times N$ pixel divisions. The coordinates of centroid $\dot{G} = \dot{G}_{ij,k\ell}$ are given by

$$\xi(\dot{G}) = \left(i - \frac{1}{2}\right)H + \left(k - \frac{1}{2}\right)h, \quad \eta(\dot{G}) = \left(j - \frac{1}{2}\right)H + \left(\ell - \frac{1}{2}\right)h. \tag{24}$$

When the transformed centroid $\dot{G} = \dot{G}_{ij,k\ell}$ falls into the standard square pixel region $\square_{IJ}$ defined in (13), the integers $(I; J)$ can be computed by

$$I = \left\lfloor x(\dot{G^*})/H + \frac{1}{2} \right\rfloor, \quad J = \left\lfloor y(\dot{G^*})/H + \frac{1}{2} \right\rfloor, \tag{25}$$

where $\lfloor x \rfloor$ is the floor function, and

$$x(\dot{G^*}) = x(\xi(\dot{G^*}), \eta(\dot{G^*})), \quad \mathrm{y}(\dot{G^*}) = y(\xi(\dot{G^*}), \eta(\dot{G^*})). \tag{26}$$

This is Step 3 in Figure 1. Equation (23) implies that the intensity values $\tilde{B}^{(N)}_{IJ}$ originate from the collective contribution of all subpixels with small subregions $\square_{ij,k\ell}$ whose centroids fall into the control region $\square_{IJ}$ of B_{IJ} in XOY. More motivation and visualization for SSM can be found in Li et al. (1989, 2004).

E. Splitting–Integrating Method for Images under T^{-1}. On the basis of intensity B_{IJ} obtained, Step 5 constructs the constant and bilinear functions $\hat{b}_\mu(x, y)$ based on an analogy of (6) and (8), where Φij is replaced by B_{IJ}, $\square_{ij}$, by $\square_{IJ}$ and $\bar{\square}_{ij}$ by $\bar{\square}_{IJ}$, defined as follows:

$$\bar{\square}_{IJ} = \left\{ \begin{array}{ll} (x,y), & IH \le x < (I+1)H \\ & JH \le y < (J+1)H \end{array} \right\}. \tag{27}$$

Then the centroid rule can easily evaluate the restored intensity (10)

$$\begin{aligned} \Phi_{ij} \approx \Phi^M_{ij} &= \frac{1}{H^2} \sum_{k,\ell=1}^{N} \iint_{\square_{ij,k\ell}} \hat{\phi}(\xi,\eta)d\xi d\eta \\ &\approx \Phi^N_{ij} = \left(\frac{h}{H}\right)^2 \sum_{k,\ell=1}^{N} \hat{\phi}(\xi(\dot{G}), \eta(\dot{G})), \end{aligned} \tag{28}$$

where $\hat{\phi}(\xi, \eta) = \hat{b}_\mu(x, y)$, $\mu = 0, 1$. This is Step 7 in Figure 1.

F. Combination of Algorithms for Images under $T^{-1}T$. Equations (23) and (28) for pixel intensity are called the splitting–shooting method (SSM) and the splitting–integrating method (SIM), respectively. The combination of SSM and SIM is referred to CSIM, as the following two cases (see Fig. 1). Case II includes Steps 1–8; Case I includes Steps 1–4 and 6–8. In Case I, the intensity B_{IJ} after Step 3 is used directly for T^{-1} without any change. Step 4 may obtain the distorted image $\{\hat{Z}\}$ from $\{\hat{B}_{IJ}\}$, but the cycle conversion does not require feedback (i.e., from Z_{IJ} to B_{IJ}, as in Step 5).

As cyclic conversion $T^{-1}T$ of images does not involve nonlinear solutions, CSIM is remarkably advantageous compared to other methods in image transformations of Dougherty and Glardina (1987), Gonzalez and Wintz (1987), Foley et al. (1990), Rogers and Adams (1990), and Pratt (1991).

III. NEW TECHNIQUES FOR PIXEL-DIVISION ALGORITHMS

A. Linear Approximation and Partition Techniques. This section describes several new approximation techniques. Split the pixel region $\bar{\square}_{ij} = \{(\xi,\eta), iH \le \xi < (i+1)H, jH \le \eta < (j+1)H\}$ by their diagonal lines into two triangles (Fig. 2): $\bar{\square}_{ij} = \bar{\Delta}_{ij,1} \cup \bar{\Delta}_{ij,2}$ and $\Omega = \cup_{ij}(\bar{\Delta}_{ij,1} \cup \bar{\Delta}_{ij,2})$. Equation (1) uses piecewise interpolation for $\phi(\xi, \eta)$, $x(\xi, \eta)$ and $y(\xi, \eta)$.

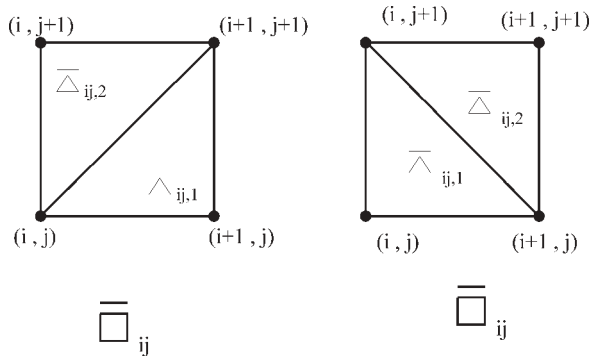

Figure 2. Triangulation on image grids.

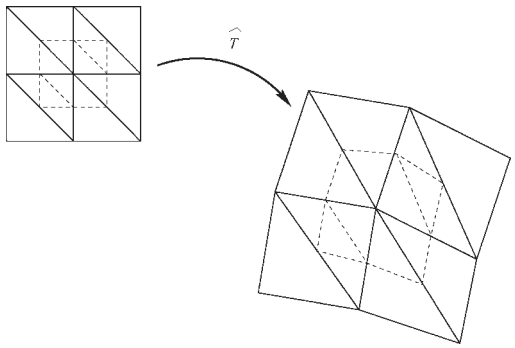

Figure 3. The piecewise linear transformation.

A.1. Technique I. Intensity Interpolation Functions. Choose piecewise constant ($\mu = 0$)

$$\hat{\phi}_0(\xi,\eta) = \phi_{ij} \quad if\,(\xi,\eta) \in \square_{ij}, \tag{29}$$

where $\square_{ij}$ is defined in (7), and piecewise linear interpolant ($\mu = 1$)

$$\hat{\phi}_1(\xi,\eta) = a_{ij,k}\xi + b_{ij,k}\eta + c_{ij,k} \quad \text{in } \bar{\Delta}_{ij,k}, k = 1,2,$$

where $\hat{\phi}_1(iH, jH) = \phi_{ij}$, and $a_{ij,k}$, $b_{ij,k}$, and $c_{ij,k}$ are constants. For the partition of the right-hand side of Figure 2, we have

$$\hat{\phi}_1(\xi,\eta) = \phi_{i,j} + \frac{(\phi_{i+1,j} - \phi_{i,j})}{H}(\xi - iH) + \frac{(\phi_{i,j+1} - \phi_{i,j})}{H}(\eta - jH),\ (\xi,\eta) \in \bar{\Delta}_{ij,1},$$

$$\hat{\phi}_1(\xi,\eta) = \phi_{i+1,j+1} - \frac{(\phi_{i+1,j} - \phi_{i+1,j+1})}{H}(\eta - (j+1)H) - \frac{(\phi_{i,j+1} - \phi_{i+1,j+1})}{H}(\xi - (i+1)H),\ \text{with}\ (\xi,\eta) \in \bar{\Delta}_{ij,2}.$$

A.2. Technique II. Piecewise Linear Approximation of T.

$$x(\xi,\eta) \approx \hat{x_1}(\xi,\eta), \quad y(\xi,\eta) \approx \hat{y_1}(\xi,\eta),$$

where the linear interpolations are exactly the same as in Technique I. Denote

$$T \approx \widehat{T} = (\xi,\eta) \to (x,y), \quad x = \hat{x}(\xi,\eta), \quad y = \hat{y}(\xi,\eta), \quad (\xi,\eta) \in \overline{\Delta}_{ij,k}. \tag{30}$$

$\widehat{T}$ denotes the piecewise linear transformation of T using the piecewise linear interpolant functions $\hat{x_1}(\xi,\eta)$ and $\hat{y_1}(\xi,\eta)$ of intensity (see Fig. 3).

A.3. Technique III. Further Partition. Choose an even division number $N(\geq N_0 \geq 2)$ to partition $\overline{\Delta}_{ij,k}$ again into $\frac{1}{2}N^2$ uniform smaller triangles (see Figs. 3 and 4): $\overline{\Delta}_{ij,k} = \bigcup_{\ell=1}^{\frac{1}{2}N^2} \overline{\Delta}_{ij,k,\ell}$ and $\overline{\Delta}_{ij,k,\ell} \xrightarrow{\widehat{T}} \overline{\Delta}^*_{ij,k,\ell}$ such that each $\overline{\Delta}^*_{ij,k,\ell}$ falls, at most, within the following four pixel regions:

$$\overline{\Delta}^*_{ij,k,\ell} \subseteq \left(\square_{IJ} \cup \square_{I+1,J} \cup \square_{I,J+1} \cup \square_{I+1,J+1}\right). \tag{31}$$

Moreover, the partition of $\overline{\Delta}^*_{ij,k,\ell} = \bigcup_m \overline{\Delta}^*_{ij,k,\ell,m}$ makes each of $\overline{\Delta}^*_{ij,k,\ell,m}$ fall into only one $\square_{IJ}$ completely. As for $\overline{\Delta}^*_{ij,k,\ell}$ only one horizontal line $y = (j + 1/2)H$ may pass through its center, the triangle $\overline{\Delta}^*_{ij,k,\ell}$ can be partitioned into at most three subtriangles in Figure 5 using the techniques of Li (1999).

$$\overline{\Delta}^*_{ij,k,\ell} = \bigcup_m \overline{\Delta}^*_{ij,k,\ell,m}, \overline{\Delta}^*_{ij,k,\ell,m} \subseteq \square_{IJ}, \tag{32}$$

where $\overline{\Delta}_{ij,k,\ell,m} \xrightarrow{\widehat{T}} \overline{\Delta}^*_{ij,k,\ell,m}$. Then, we have $\overline{\square}_{ij} = \bigcup_{\ell,m} (\overline{\Delta}_{ij,1,\ell,m} \cup \overline{\Delta}_{ij,2,\ell,m})$.

B. Algorithm NSSM for *T* with μ = 0, 1. First, let us give a lemma.

Lemma 3.1. *Let* Δ_{abc} *be a triangle, and* $f(\xi, \eta)$ *be linear functions. Then, the centroid rule has no errors (see Fig. 6):*

$$\iint_{\Delta_{\text{abc}}} f(\xi,\eta)d\xi d\eta = \text{Area}(\Delta_{\text{abc}}) f(\xi_e, \eta_e), \tag{33}$$

where e is the centroid of Δ_{abc}.

Proof. Denote a reference triangle $\overline{\Delta} = \{(x,y) | 0 \leq x \leq 1, 0 \leq y \leq 1 - x\}$, and choose the linear function $\overline{f} = a + bx + cy$ on $\overline{\Delta}$ with constants a, b, and c. Determine the exact values of integration by calculus,

$$\iint_{\overline{\Delta}} \overline{f} = \int_0^1 dx \int_0^{1-x} (a + bx + cy)dy = a\int_0^1 (1-x)dx + b\int_0^1 (1-x)dx + \frac{c}{2}\int_0^1 (1-x)^2 dx = \frac{a}{2} + \frac{b+c}{6}. \tag{34}$$

As $\text{Area}(\overline{\Delta}) = \frac{1}{2}$, and the centroid coordinates of $\overline{\Delta}$ are $(x_e, y_e) = \left(\frac{1}{3}, \frac{1}{3}\right)$, the centroid rule gives

$$\iint_{\overline{\Delta}} \overline{f} = \text{Area}(\overline{\Delta}) \overline{f}(\overline{x}_e, \overline{y}_e) = \frac{1}{2} \cdot \left(a + \frac{1}{3}(b+c)\right) = \frac{a}{2} + \frac{b+c}{6}. \tag{35}$$

From Eqs. (34) and (35),

$$\iint_{\overline{\Delta}} \overline{f} = \iint_{\overline{\Delta}} \overline{f} \tag{36}$$

From Li et al. (1989), under a linear transformation, the linear function is still linear, the triangle is also a triangle, and its centroid remains the same. As the transformation from Δ_{abc} to $\overline{\Delta}$ is a linear transformation (Li et al., 1989), the centroid rule in (33) on a triangle is exactly the same as that for linear functions. This completes the proof of Lemma 3.1. □

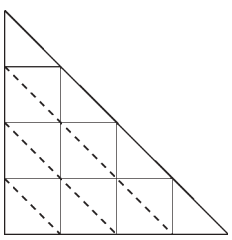

Figure 4. $N = 4$ in triangulation of $\Delta_{ij,1}$ and $\overline{\Delta}_{ij,1}$ in Figure 2.

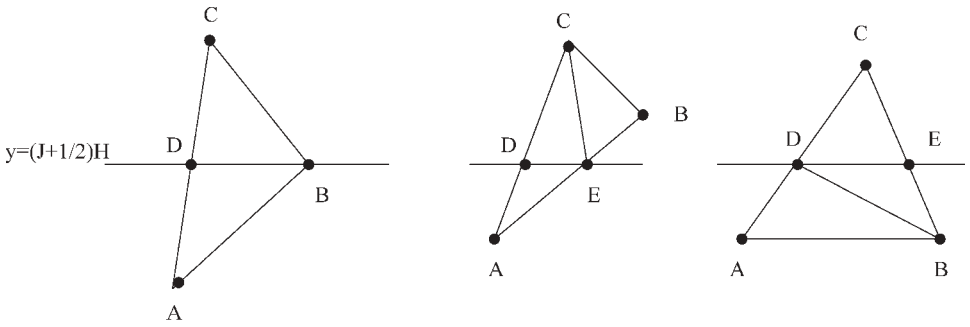

Figure 5. Three cases of dividing ΔABC by the horizontal line $y = \left(J + \frac{1}{2}\right)H$.

The techniques in Section A (subsection of Section III) can then obtain the approximate integrals for the transformation $\widehat{T}$,

$$B_{IJ} = \frac{1}{H^2}\iint_{\Omega_{IJ}} \phi(\xi,\eta)\vartheta(\xi,\eta)d\xi d\eta \approx$$
$$\widehat{B}_{IJ} = \frac{1}{H^2}\iint_{\Omega_{IJ}} \widehat{\phi}(\xi,\eta)\widehat{\vartheta}(\xi,\eta)d\xi d\eta,$$

where $\square_{IJ} \xrightarrow{T} \Omega_{IJ}$, and $\square_{IJ} \xrightarrow{\widehat{T}} \widehat{\Omega}_{IJ}$. The Jacobian determinants are defined by

$$\vartheta = \begin{vmatrix} \frac{\partial x}{\partial \xi} & \frac{\partial x}{\partial \eta} \\ \frac{\partial y}{\partial \xi} & \frac{\partial y}{\partial \eta} \end{vmatrix}, \quad \widehat{\vartheta} = \begin{vmatrix} \frac{\partial \widehat{x}}{\partial \xi} & \frac{\partial \widehat{x}}{\partial \eta} \\ \frac{\partial \widehat{y}}{\partial \xi} & \frac{\partial \widehat{y}}{\partial \eta} \end{vmatrix},$$

and $\widehat{\vartheta}$ is constant in $\overline{\Delta}_{ij,k}$ due to linear transformations. For $\mu = 0,1$,

$$\Omega_{IJ} \approx \widehat{\Omega}_{IJ} = \bigcup_{\substack{\forall ij,k,\ell,m \\ \text{satisfying(38)}}} \left(\overline{\Delta}_{ij,k,\ell,m}\right). \tag{37}$$

and

$$\overline{\Delta}_{ij,k,\ell,m} \xrightarrow{\widehat{T}} \overline{\Delta}^*_{ij,k,\ell,m},\ \overline{\Delta}^*_{ij,k,\ell,m} \subseteq \square_{IJ}. \tag{38}$$

Denote the center of gravity of $\overline{\Delta}_{ij,k,\ell,m}$ by $\left(x_{\dot{g}}, y_{\dot{g}}\right)$, where $x_{\dot{g}} = x_{\dot{g}_{ij,k,\ell,m}}$ and $y_{\dot{g}} = y_{\dot{g}_{ij,k,\ell,m}}$. Then, for the inverse transformation under $\widehat{T}^{-1} : (x_{\dot{g}}, y_{\dot{g}}) \xrightarrow{\widehat{T}^{-1}} (\widehat{\xi}_{\dot{g}}, \widehat{\eta}_{\dot{g}})$, their coordinates $\widehat{\xi}_{\dot{g}}$ and $\widehat{\eta}_{\dot{g}}$ can be obtained by the area coordinates directly. Hence, we obtain from Lemma 3.1

$$\begin{aligned} \widehat{B}_{IJ} &= \frac{1}{H^2}\iint_{\widehat{\Omega}_{IJ}} \widehat{\phi}_\mu(\xi,\eta)\widehat{\vartheta}(\xi,\eta)d\xi d\eta \\ &= \frac{1}{H^2} \sum_{\substack{\forall ij,k,\ell,m \\ \text{satisfying(38)}}} \iint_{\overline{\Delta}^*_{ij,k,\ell,m}} \widehat{\phi}_\mu(\xi,\eta)dxdy \\ &= \frac{1}{H^2} \sum_{\substack{\forall ij,k,\ell,m \\ \text{satisfying(38)}}} \widehat{\phi}_\mu(\widehat{\xi}_{\dot{g}}, \widehat{\eta}_{\dot{g}})\text{Area}(\overline{\Delta}^*_{ij,k,\ell,m}). \end{aligned} \tag{39}$$

As the inverse functions in linear transformations are still linear, functions $\widehat{\phi}_\mu(\xi,\eta)$ on $\overline{\Delta}^*_{ij,k,\ell,m}$ are also linear. On the basis of Lemma 3.1, the center rule of integration offers no error at all, and the integration evaluation in (39) is exact!

C. Algorithm NSIM for T^{-1} with $\mu = 0$. This section considers the inverse transformation T^{-1} by NSIM with $\mu = 0$. Similarly,

$$\phi_{ij} = \frac{1}{H^2}\iint_{ij} b(\xi,\eta)d\xi d\eta \approx \widehat{\phi}_{ij} = \frac{1}{H^2}\iint_{ij} \widehat{b}_0(\xi,\eta), \widehat{y}(\xi,\eta)d\xi d\eta. \tag{40}$$

As $N(\geq 2)$ is even and $\square_{ij} = \cup_{k,\ell,m}\Delta_{ij,k,\ell,m}, \exists \overline{ij}$ such that $\Delta_{ij,k,\ell,m} \in \overline{\Delta}_{\overline{ij},\ell}$, where $\overline{\Delta}_{ij,\ell}$ with $\overline{i} = i$ and $\overline{j} = j$, as Figure 2. We have from Lemma 3.1

$$\begin{aligned} \widehat{\phi}_{ij} &= \frac{1}{H^2}\iint_{\square_{ij}} \widehat{b}_0(\widehat{x}(\xi,\eta), \widehat{y}(\xi,\eta))d\xi d\eta \\ &= \frac{1}{H^2}\sum_{k,\ell,m}\iint \widehat{b}_0(\widehat{\xi}_{\dot{g}}, \widehat{\eta}_{\dot{g}})\text{Area}(\Delta_{ij,k,\ell,m}), \end{aligned} \tag{41}$$

where $(\widehat{\xi}_{\dot{g}}, \widehat{\eta}_{\dot{g}})$ are the coordinates of the centroid of $\Delta_{ij,k,\ell,m}$. When $N \geq N_0$, the evaluation of $\widehat{\phi}_{ij}$ by (41) is also exact.

Note that for $\mu = 1$, different but more complicated partitions on $\Delta_{ij,k,\ell}$ into more subtriangles are required for T^{-1} to avoid sequential errors. For the new algorithms without sequential errors when $N(\geq N_0 \geq 2)$, denote the new splitting–shooting method by NSSM for T with $\mu = 0$, 1, the new splitting–integrating method by NSIM for T^{-1} with $\mu = 0$, and the new combination of splitting–shooting and splitting–integrating methods by NCSIM for $T^{-1}T$. Let $N = 2^p$ and $N_0 = 2^p$, $p_0 \geq 1$. As each of $\overline{\Delta}^*_{ij,k,\ell,m}$ falls into one $\square_{IJ}$ completely, different divisions $N(\geq N_0)$ do not change the intensity values of $\widehat{B}_{IJ}$ in (39) and $\widehat{\phi}_{ij}$ in (41). This is a significant improvement over the results presented in Li (1989, 1990, 1994, 1996, 1999, 1998, 2001, 2004).

Remark 3.1. Figure 7 illustrates the linkage among the Area Method (Li, 1990), CSIM in Li (1990), ACSIM in Li, (1999), and

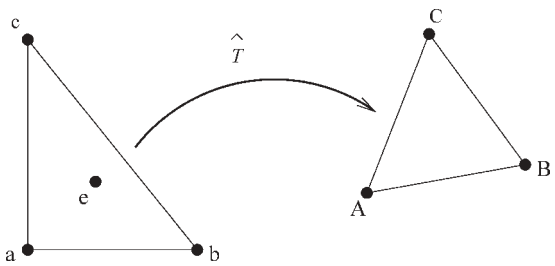

Figure 6. Triangle Δabc under $\widehat{T}$.

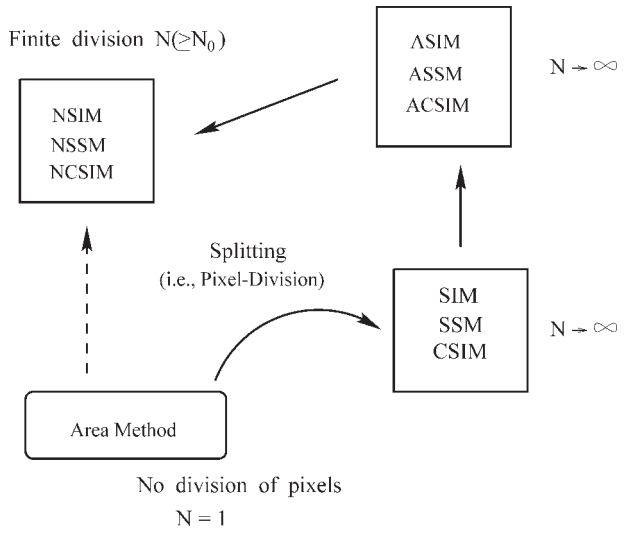

Figure 7. The relationship among the Area Method, CSIM, ACSIM, and NCSIM in this article.

NCSIM in this article. In NCSIM, a preliminary partition with $N(\geq N_0 \geq 2)$ on $\overline{\square}_{ij}$ is still required to locate $\overline{\Delta}^{*}_{ij,k,\ell,m} \subseteq \square_{IJ}$. Interestingly, the splitting algorithms in this article mimic the Area Method in Li (1990) for nonlinear transformations T, but use a smaller pixel division $N \geq N_0$.

IV. ERROR ANALYSIS FOR IMAGES WITH DISCONTINUOUS INTENSITY

The brief error analysis in this section indicates that true errors of image intensity under transformations by the new splitting algorithms in Section III have the order $O(H)$. This significance of order $O(H)$ is valid for images with all kinds of discontinuous intensity. The transformation T is regular, if the following conditions are satisfied (see Li and Bai, 1998): $x(\xi, \eta), y(\xi, \eta) \in C^2(\Omega)$ and

$$0 < \vartheta_0 \leq \vartheta(\xi, \eta) = \left| \begin{matrix} \frac{\partial x}{\partial \xi} & \frac{\partial x}{\partial \eta} \\ \frac{\partial y}{\partial \xi} & \frac{\partial y}{\partial \eta} \end{matrix} \right| \leq \vartheta_M.$$

A. For Intensity Values of Images by NSSM for *T*. This section provides the following lemmas, but omits the proof for the sake of brevity.

Lemma 4.1. *Let T be regular, and let $\hat{x}(\xi, \eta)$ be the piecewise linear interpolants of $x(\xi, \eta)$. Then, there exist the error bounds,*

$$|x(\xi, \eta) - \hat{x}(\xi, \eta)| \leq CM_2H^2, \quad \left| \frac{\partial x}{\partial \xi} - \frac{\partial \hat{x}}{\partial \hat{\xi}} \right| \leq CM_2H,$$

where C is a positive constant independent of H, and

$$M_k = |x|_{k,\infty,\Omega} + |y|_{k,\infty,\Omega}, \quad |v|_{k,\infty,\Omega} = \max_{\substack{|\alpha|=k \\ in\ \Omega}} |D^{\alpha} v|,$$

where the function $v(\xi, \eta) \in \Omega$.

The arguments in Li (1999) lead to the following lemma.

Lemma 4.2. *Let T be regular, and let $\hat{T}$ be its piecewise linear approximation on $\Delta_{ij,k}$. For $\square_{ij} \xrightarrow{T} S_{ij}$ and $\square_{ij} \xrightarrow{\hat{T}} \hat{S}_{ij}$ (see Fig. 8), the area differences between Sij and $\hat{S}_{ij}$ have the bound*

$$|S_{ij} \oplus \hat{S}_{ij}| \leq CH^3 \vartheta_M^{1/2} M_2.$$

For $\square_{IJ} \xrightarrow{T^{-1}} \Omega_{IJ}$ and $\square_{IJ} \xrightarrow{\hat{T}^{-1}} \hat{\Omega}_{IJ}$,

$$|\Omega_{IJ} \oplus \hat{\Omega}_{IJ}| \leq CH^3 \frac{M_2^*}{\vartheta_0^{1/2}},$$

where $p \oplus q$ denotes the exclusive OR of p and q. Hence, $S_{ij} \oplus \hat{S}_{ij}$ denotes the difference in area between S_{ij} and $\hat{S}_{ij}$, C is a positive constant independent of H, and

$$M_k^* = |\xi|_{k,\infty,S} + |\eta|_{k,\infty,S}, \quad |v|_{k,\infty,S} = \max_{\substack{|\alpha|=k \\ in\ s}} |D^{\alpha} v|$$

Now let us prove the main theorem, to show the error bounds $O(H)$ of intensity values.

Theorem 4.1. *Let T be regular. Then, the intensity $\hat{B}_{IJ}$ under T by NSSM in (39) has the error bounds for $\mu = 0$ or 1*

$$|B_{IJ}^{+} - \hat{B}_{IJ}| \leq CH \left[\frac{M_2^* \vartheta_M}{\vartheta_0^{\frac{1}{2}}} + \frac{M_1 M_2}{\vartheta_0} \right], \tag{42}$$

where

$$B_{IJ}^{+} = \frac{1}{H^2} \iint_{\Omega_{IJ}} \hat{\phi}_{\mu}(\xi, \eta) \vartheta(\xi, \eta) d\xi d\eta. \tag{43}$$

Proof. We have

$$|B_{IJ}^{+} - \hat{B}_{IJ}| \leq \frac{1}{H^2} \left\{ \iint_{\Omega_{IJ} \oplus \hat{\Omega}_{IJ}} \hat{\phi}_{\mu}(\xi, \eta) \vartheta(\xi, \eta) d\xi d\eta + \iint_{\Omega_{IJ}} \hat{\phi}_{\mu}(\xi, \eta) |\vartheta(\xi, \eta) - \hat{\vartheta}(\xi, \eta)| d\xi d\eta \right\} \tag{44}$$

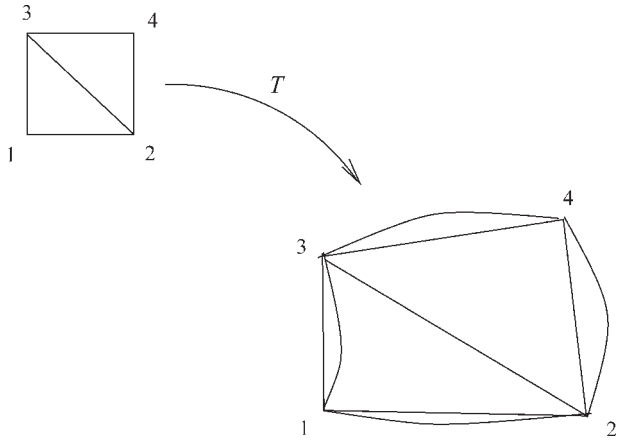

Figure 8. The pixel region $\square_{ij}$ and the distorted regions S_{ij} and $\widehat{S_{ij}}$, where $\square_{ij} \to S_{ij}$ by T and $\square_{ij} \to \widehat{S_{ij}}$ by $\hat{T}$.

From Lemma 4.2, $|\hat{\phi}_\mu(\xi,\eta)| \le 1$ and $|\vartheta(\xi,\eta)| \le \vartheta_M$, it follows that

$$\frac{1}{H^2}\iint_{\Omega_{IJ}\oplus\widehat{\Omega}_{IJ}} \widehat{\phi}_\mu(\xi,\eta)\vartheta(\xi,\eta)d\xi d\eta \le CHM_2^*\frac{\vartheta_M}{\vartheta_0^{1/2}} \tag{45}$$

Also, we have from Lemma 4.1,

$$\left|\vartheta(\xi,\eta)-\widehat{\vartheta}(\xi,\eta)\right| = \left|\left|\begin{matrix}\frac{\partial x}{\partial\xi} & \frac{\partial x}{\partial\eta}\\ \frac{\partial y}{\partial\xi} & \frac{\partial y}{\partial\eta}\end{matrix}\right| - \left|\begin{matrix}\frac{\partial\widehat{x}}{\partial\xi} & \frac{\partial\widehat{x}}{\partial\eta}\\ \frac{\partial\widehat{y}}{\partial\xi} & \frac{\partial\widehat{y}}{\partial\eta}\end{matrix}\right|\right| \tag{46}$$

$$\le \left|\frac{\partial x}{\partial\xi}\left(\frac{\partial y}{\partial\eta}-\frac{\partial\widehat{y}}{\partial\eta}\right)\right| + \left|\frac{\partial\widehat{y}}{\partial\eta}\left(\frac{\partial x}{\partial\xi}-\frac{\partial\widehat{x}}{\partial\xi}\right)\right| + \left|\frac{\partial x}{\partial\eta}\left(\frac{\partial y}{\partial\xi}-\frac{\partial\widehat{y}}{\partial\xi}\right)\right|$$
$$+ \left|\frac{\partial\widehat{y}}{\partial\xi}\left(\frac{\partial x}{\partial\eta}-\frac{\partial\widehat{x}}{\partial\eta}\right)\right| \le CHM_1M_2.$$

Hence, we obtain

$$\begin{aligned}&\frac{1}{H^2}\iint_{\widehat{\Omega}_{IJ}} \widehat{\phi}_\mu(\xi,\eta)\left|\vartheta(\xi,\eta)-\widehat{\vartheta}(\xi,\eta)\right|d\xi d\eta\\ &\le CHM_1M_2\left\{\frac{1}{H^2}\iint_{\widehat{\Omega}_{IJ}} d\xi d\eta\right\} \le C\frac{H}{\vartheta_0}M_1M_2,\end{aligned} \tag{47}$$

where we have used the bound for $\square_{IJ} \xrightarrow{\widehat{T}^{-1}} \widehat{\Omega}_{IJ} \xrightarrow{T} \widehat{\square}_{IJ} \approx \square_{IJ}$,

$$\frac{1}{H^2}\iint_{\widehat{\Omega}_{IJ}} d\xi d\eta \le \frac{1}{\vartheta_0 H^2}\iint_{\widehat{\Omega}_{IJ}} \vartheta d\xi d\eta = \frac{1}{\vartheta_0 H^2}\iint_{\widehat{\square}_{IJ}} dxdy \le \frac{C}{\vartheta_0}. \tag{48}$$

Combining (44), (45), and (47) yields (42). This completes the proof. □

B. For Intensity Values of Images by NSIM for T^{-1}. Next, consider the inverse transformation, for which we have the following theorem.

Theorem 4.2. *Let T be regular. Then, the intensity $\hat{\phi}_{ij}$ under T^{-1} by NSIM for $\mu = 0$ in (41) has the error bound,*

$$\left|\phi_{ij}^+ - \widehat{\phi}_{ij}\right| \le C\frac{HM_2}{\vartheta_0}(\vartheta_M^{1/2}+M_1), \tag{49}$$

where

$$\phi_{ij}^+ = \frac{1}{H^2}\iint_{ij} \widehat{b}_0(x(\xi,\eta),y(\xi,\eta))d\xi d\eta. \tag{50}$$

Proof. For $\square_{ij} \xrightarrow{T} S_{ij}$ and $\square_{ij} \xrightarrow{\widehat{T}} \widehat{S}_{ij}$ shown in Figure 8, we have

$$\begin{aligned}|\phi_{ij}^+ - \widehat{\phi}_{ij}| &= |\frac{1}{H^2}\iint_{S_{ij}} \widehat{b}_0(x(\xi,\eta),y(\xi,\eta))\vartheta^{-1}dxdy\\ &\quad -\frac{1}{H^2}\iint_{\widehat{S}_{ij}} \widehat{b}_0(\widehat{x}(\xi,\eta),\widehat{y}(\xi,\eta))\widehat{\vartheta}^{-1}dxdy|\\ &\le \frac{1}{H^2}|\iint_{S_{ij}\oplus\widehat{S}_{ij}} \widehat{b}_0(x(\xi,\eta),y(\xi,\eta))\vartheta^{-1}dxdy|\\ &\quad + \frac{1}{H^2}|\iint_{\widehat{S}_{ij}} (\widehat{b}_0(x(\xi,\eta),y(\xi,\eta)) - \widehat{b}_0(\widehat{x}(\xi,\eta),\widehat{y}(\xi,\eta)))\vartheta^{-1}dxdy|\\ &\quad + \frac{1}{H^2}|\iint_{\widehat{S}_{ij}} \widehat{b}_0(\widehat{x}(\xi,\eta),\widehat{y}(\xi,\eta))(\vartheta^{-1}-\widehat{\vartheta}^{-1})dxdy|.\end{aligned} \tag{51}$$

Later, we estimate three terms on the most right-hand side of (51). As $0 \le \widehat{b}_0 \le 1$, we have from Lemma 4.2

$$\begin{aligned}&\frac{1}{H^2}\iint_{S_{ij}\oplus\widehat{S}_{ij}} \widehat{b}_0(x(\xi,\eta),y(\xi,\eta))\vartheta^{-1}dxdy\\ &\le \frac{1}{H^2}\iint_{S_{ij}\oplus\hat{S}_{ij}} \vartheta^{-1}dxdy\\ &\le \frac{1}{\vartheta_0 H^2}|S_{ij}\oplus\hat{S}_{ij}| \le \frac{CH}{\vartheta_0}\vartheta_M^{1/2}M_2.\end{aligned} \tag{52}$$

Second, we have

$$\begin{aligned}&\frac{1}{H^2}|\iint_{\hat{S}_{ij}} |\hat{b}_0(x(\xi,\eta),y(\xi,\eta)) - \hat{b}_0(\hat{x}(\xi,\eta),\hat{y}(\xi,\eta))\vartheta^{-1}dxdy|\\ &\le \frac{1}{\vartheta_0 H^2}|\iint_{\hat{S}_{ij}} |\hat{b}_0(x(\xi,\eta),y(\xi,\eta)) - \hat{b}_0(\hat{x}(\xi,\eta),\hat{y}(\xi,\eta))|dxdy.\end{aligned} \tag{53}$$

Note that $\widehat{b}_0$ is piecewise constant on $\bigcup_{IJ}\square_{IJ}$ based on the pixel intensity B_{IJ} of the distorted image. Figure 8 shows that the differences between $\widehat{b}_0(x(\xi,\eta),y(\xi,\eta))$ and $\widehat{b}_0(\hat{x}(\xi,\eta),\hat{y}(\xi,\eta))$ occur only on $S_{ij}\oplus\widehat{S}_{ij}$, which overlaps the boundary of $\square_{IJ}$ and whose neighboring pixel intensities in B_{IJ} are different. Hence, we have from Lemma 4.2

$$\begin{aligned}&\iint_{\hat{S}_{ij}} |\hat{b}_0(x(\xi,\eta),y(\xi,\eta)) - \hat{b}_0(\hat{x}(\xi,\eta),\hat{y}(\xi,\eta))|dxdy\\ &\le C|S_{ij}\oplus\hat{S}_{ij}| \le CH^3\vartheta_M^{1/2} + M_2.\end{aligned} \tag{54}$$

From (53) and (54), the second term on the most right-hand side of (51) leads to

$$\begin{aligned}&\frac{1}{H^2}|\iint_{\hat{S}_{ij}} (\hat{b}_0(x(\xi,\eta),y(\xi,\eta)) - \hat{b}_0(\hat{x}(\xi,\eta),\hat{y}(\xi,\eta)))\vartheta^{-1}dxdy|\\ &\le \frac{CH}{\vartheta_0}\vartheta_M^{1/2}M_2.\end{aligned} \tag{55}$$

Third, we have from (46)

$$\begin{aligned}&\frac{1}{H^2}|\iint_{\hat{S}_{ij}} \hat{b}_0(\hat{x}(\xi,\eta),\hat{y}(\xi,\eta))(\vartheta^{-1}-\widehat{\vartheta}^{-1})dxdy|\\ &\le \frac{1}{H^2}|\iint_{\widehat{S}_{ij}} \frac{\widehat{\vartheta}-\vartheta}{\widehat{\vartheta}}\vartheta^{-1}dxdy|\\ &\le C\frac{\max|\widehat{\vartheta}-\vartheta|}{\vartheta_0}\left\{\frac{1}{H^2}\iint_{\widehat{S}_{ij}} \vartheta^{-1}dxdy\right\}\\ &\le C\frac{\max|\widehat{\vartheta}-\vartheta|}{\vartheta_0}\left\{\frac{1}{H^2}\iint_{\widehat{\square}_{ij}} d\xi d\eta\right\} \le C\frac{HM_1M_2}{\vartheta_0},\end{aligned} \tag{56}$$

where $\square_{ij} \xrightarrow{T} \widehat{S}_{ij} \xrightarrow{\widehat{T}^{-1}} \widehat{\square}_{ij} \approx \square_{ij}$.

Finally, combining (51), (52), (55), and (56) yields

$$\begin{aligned}\left|\phi_{ij}^+ - \phi_{ij}^-\right| &\le C\left\{\frac{H}{\vartheta_0}\vartheta_M^{1/2}M_2 + \frac{H}{\vartheta_0}M_1M_2\right\}\\ &= C\frac{HM_2}{\vartheta_0}(\vartheta_M^{1/2}+M_1).\end{aligned}$$

This completes the proof. □

C. For Intensity Values of Images by NCSIM for $T^{-1}T$. On the basis of Theorems 4.1 and 4.2, it is relatively easy to obtain the true error bounds $E = O(H)$ of intensity of the entire image under geometric transformations. Error analysis can also be applied to images with discontinuous intensity.

This subsection first defines some error norms to measure the degree of approximation of intensity solutions. Choose the division number

$$N = N_p = 2^{p+k}, \text{ where } p = 0, 1, \ldots, \text{ and integer } k > 0 \tag{57}$$

Now, consider the images under the cyclic transformation $T^{-1}T$. Define the sequential errors of image intensity under T^{-1} or $T^{-1}T$ with the two division numbers N_p and N_{p-1}:

$$\begin{aligned} \Delta E^{(N_p)}(\tilde{\Phi}) &= \sum_{ij} \frac{\left|\tilde{\Phi}_{ij}^{(N_p)} - \tilde{\Phi}_{ij}^{(N_{p-1})}\right|}{I_{\max}(\tilde{W})}, \\ \Delta E_2^{(N_p)}(\tilde{\Phi}) &= \left\{ \sum_{ij} \frac{\left(\tilde{\Phi}_{ij}^{(N_p)} - \tilde{\Phi}_{ij}^{(N_{p-1})}\right)^2}{I_{\max}(\tilde{W})} \right\}^{1/2}, \end{aligned} \tag{58}$$

where $I_{\max}(\tilde{W})$ is the total number of image pixels, defined by

$$I_{\max}(\tilde{W}) = \sum_{ij} N_f(\tilde{W}_{ij}^{(N_p)}), \quad N_f(W_{ij}) = \begin{cases} 1 & \text{if } W_{ij} \neq '\,'; \\ 0 & \text{if } W_{ij} = '\,'. \end{cases} \tag{59}$$

In fact, the errors in (58) are defined for the mean and the standard deviation of intensity errors. Moreover, as the original values Φ_{ij} are known in the cyclic transformation $T^{-1}T$, we can also compute the true errors and the standard deviations by

$$E^{(N_p)}(\tilde{\Phi}) = \sum_{ij} \frac{\left|\tilde{\Phi}_{ij}^{(N_p)} - \Phi_{ij}\right|}{I_{\max}(\tilde{W})}, \quad E_2^{(N_p)}(\tilde{\Phi}) = \left\{ \sum_{ij} \frac{(\tilde{\Phi}_{ij}^{(N_p)} - \tilde{\Phi}_{ij})^2}{I_{\max}(\tilde{W})} \right\}^{1/2}. \tag{60}$$

Similarly, define the sequential errors of image intensity under T

$$\begin{aligned} \Delta E^{(N_p)}(\tilde{B}) &= \sum_{IJ} \frac{\left|\tilde{B}_{IJ}^{(N_p)} - B_{IJ}^{(N_{p-1})}\right|}{I_{\max}(\tilde{Z})}, \\ \Delta E_2^{(N_p)}(\tilde{B}) &= \left\{ \sum_{ij} \frac{(\tilde{B}_{ij}^{(N_p)} - B_{ij}^{(N_{p-1})})^2}{I_{\max}(\tilde{Z})} \right\}^{1/2}, \end{aligned} \tag{61}$$

$$E^{(N_p)}(\tilde{B}) = \sum_{IJ} \frac{\left|\tilde{B}_{IJ}^{(N_p)} - B_{IJ}\right|}{I_{\max}(\tilde{Z})}, \quad E_2^{(N_p)}(\tilde{B}) = \left\{ \sum_{ij} \frac{(\tilde{B}_{ij}^{(N_p)} - B_{ij})^2}{I_{\max}(\tilde{Z})} \right\}^{1/2}, \tag{62}$$

where $I_{\max}(\tilde{Z}) = \sum_{IJ} N_f(\tilde{Z}_{IJ}^{(N_p)})$.

Theorem 4.3. *Let $\phi(\xi, \eta) \in C^2(\Omega)$, (57), and all conditions in Theorems 4.1 and 4.2 hold. There exists a small division number $N_0 \geq 2$* such that for $p \geq 0$, *the error norms in (58)–(61) satisfy the following relations:*

$$\Delta E^{(N_p)}(\tilde{\Phi}) = 0, \tag{63}$$

$$E^{(N_p)}(\tilde{\Phi}) = O(H), \tag{64}$$

$$\Delta E^{(N_p)}(\tilde{B}) = 0, \tag{65}$$

$$E^{(N_p)}(\tilde{B}) = O(H). \tag{66}$$

Proof. This article only proves (65) and (66), as the proofs for (63) and (64) are similar. On the basis of Theorem 4.1, when $N_{p-1} \geq N_0$ for $p \geq 1$, the values of $\tilde{B}_{IJ}^{N_{p-1}}$ and $\tilde{B}_{IJ}^{N_p}$ remain the same, that is,

$$\tilde{B}_{IJ}^{N_{p-1}} = \tilde{B}_{IJ}^{N_p}, \quad p \geq 1.$$

This is (65) by noting the definition in (61).

Next, we have

$$\left|\tilde{B}_{IJ}^{N_p} - B_{IJ}\right| \leq \left|\tilde{B}_{IJ}^{N_p} - B_{IJ}^{+}\right| + \left|B_{IJ} - B_{IJ}^{+}\right|, \tag{67}$$

where B_{IJ} and B_{IJ}^{+} are defined in (16) and (43), respectively. Letting $\tilde{B}_{IJ}^{N_p} = \hat{B}_{IJ}$ in (39), we have from Theorem 4.1

$$\left|\tilde{B}_{IJ}^{N_p} - B_{IJ}^{+}\right| \leq CH\left[\frac{M_2^* \vartheta_M}{\vartheta_0^{\frac{1}{2}}} + \frac{M_1 M_2}{\vartheta_0}\right], \quad p \geq 1. \tag{68}$$

Moreover, it follows from (16) and (43) that

$$\begin{aligned} \left|B_{IJ}^{N_p} - B_{IJ}^{+}\right| &= \frac{1}{H^2}\left|\iint_{\Omega_{IJ}} (\phi_\mu(\xi, \eta) - \hat{\phi}_\mu(\xi, \eta)\vartheta(\xi, \eta) d\xi d\eta)\right| \\ &\leq \max_{(\xi,\eta\in\Omega)}\left|\phi_\mu(\xi, \eta) - \hat{\phi}_\mu(\xi, \eta)\right| \times \left\{\frac{1}{H^2}\left|\iint_{\Omega_{IJ}} \vartheta(\xi, \eta) d\xi d\eta\right|\right\}. \end{aligned} \tag{69}$$

As $\phi \in C^2(\Omega)$, there exists the bound,

$$\max_{(\xi,\eta\in\Omega)}\left|\phi_\mu(\xi, \eta) - \hat{\phi}_\mu(\xi, \eta)\right| \leq CH^{\mu+1} M_{\mu+1}, \quad \mu = 0.1, \tag{70}$$

where C is a constant independent of H. We have

$$\frac{1}{H^2}\left|\iint_{\Omega_{IJ}} \vartheta(\xi, \eta) d\xi d\eta\right| = \frac{1}{H^2}\left|\iint_{\square_{IJ}} dxdy\right| = 1. \tag{71}$$

Combining (69)–(71) gives

$$\left|\tilde{B}_{IJ}^{N_p} - B_{IJ}^{+}\right| \leq CH^{u+1} M_{u+1}, \quad \mu = 0, 1. \tag{72}$$

Finally, we obtain from (67), (68), and (71)

$$\left|\tilde{B}_{IJ}^{N_p} - B_{IJ}\right| \leq CH\left[\frac{M_2^* \vartheta_M}{\vartheta_0^{\frac{1}{2}}} + \frac{M_1 M_2}{\vartheta_0} + H^\mu M_{\mu+1}\right] = \mathrm{O(H)}, \ \mu = 0, 1. \tag{73}$$

Figure 9. Standard images of public data, such as Lena, Baboon, Boots, and Pepper, each with 256 × 256 pixels and 256 intensity levels.

Hence we have

$$\mathrm{E}^{(N_p)}(\tilde{B}) = \sum_{IJ} \frac{\left|\tilde{B}_{IJ}^{(N_p)} - B_{IJ}\right|}{I_{\max}(\tilde{Z})} = O(H). \tag{74}$$

This is (66) and completes the proof. □

The errors $\Delta E2$ and $E2$ of the standard deviation as in (58)–(62) produce the same conclusions as those in Theorem 4.3.

V. NUMERICAL EXPERIMENTS

This section first validates the algorithms in Section III, where the intensity evaluation on $\hat{T}$ is unchangeable when N, $N0$, 2, to illustrate the effectiveness of the proposed algorithms, and to verify the error analysis in Section IV.

A. The Perspective Model. From the application viewpoint, we choose the perspective images to validate the new algorithms. Suppose that the original figures are embedded in the square $\Omega\{(\bar{\xi}, \bar{\eta}), 1 \le \bar{\xi} \le 256, 1 \le \bar{\eta} \le 256\}$ on $\xi O\eta$. We construct Ω upright and rotate it along axis η with angle $\frac{\pi}{9}$. The coordinates of the original plane are then given by

$$\begin{cases} \xi = \bar{\xi}\cos\frac{\pi}{9}, \\ \eta = \bar{\eta}\sin\frac{\pi}{9}, \\ \xi = \bar{\eta}. \end{cases}$$

We choose the perspective plane as $y = 400$, and the coordinates of the origin of xyz at (50, 512, 200), and obtain from Li et al. (1989) a transformation from the original 2D point to another 2D point.

$$\bar{T} : (\bar{\xi}, \bar{\eta}) \to (x, y),$$

where

$$x = 400\frac{\bar{\xi}\cos\frac{\pi}{9} + 50}{\bar{\xi}\sin\frac{\pi}{9} + 512}, \quad y = 400\frac{\bar{\eta} + 200}{\bar{\xi}\sin\frac{\pi}{9} + 512}. \tag{75}$$

The above transformation $\bar{T}$ is called the perspective transformation.

B. Computational Experiments. Choose the standard test images of 256 × 256 pixels with 256 intensity levels in Figure 9. For the perspective transformation, use the NSSM for T for $\mu = 0$ or 1, and then use NSIM for T^{-1} for $\mu = 0$. When $N = 2^{\mathrm{p}}$, Tables I and II list the numerical errors, where $\Delta P{\cdot}E$ and $P{\cdot}E$ denote the sequential pixel errors and the true pixel errors, respectively. Note that the $\Delta P{\cdot}E$ in T for $\mu = 0$ or 1 remains unchanged as ($N \ge N_0$) increases, based on the analysis in Section IV. These tables show that the $\Delta P{\cdot}E$ in $T^{-1}T$ do not change. Finally, Figures 10 and 11 show the images using NSSM for T for $\mu = 0$ or 1 and NSIM for T^{-1} for $\mu = 0$. According to Tables I and II, the maximal pixel errors for the restored images are less than 12 intensity levels. These errors are so small in a system of 256 intensity levels that the naked eye can hardly perceive the differences between the original and restored images in Figures 9–11.

C. Harmonic Transformations. The following presents some applications of the algorithms for the transformations of harmonic

Table 1. The numerical errors of images by *NSSM* with $\mu = 0$ for T, and then by *NSIM* with $\mu = 0$ for T^{-1} under the perspective transformation

		T		$T^{-1}T$		True	
Items	N	$\Delta P.E.$	ΔE	$\Delta P.E.$	ΔE	$P.E.$	E
Lena	2	–	–	–	–	5.181	2.013 E-2
	4	1.448 E-4	1.974 E-15	3.052 E-5	1.745 E-7	5.181	2.013 E-2
	8	1.158 E-4	3.863 E-15	0	4.380 E-8	5.181	2.013 E-2
Baboon	2	–	–	–	–	11.372	4.452 E-2
	4	0	2.513 E-15	7.629 E-5	3.457 E-7	11.372	4.452 E-2
	8	0	4.888 E-15	3.052 E-5	8.665 E-8	11.372	4.452 E-2
Boots	2	–	–	–	–	8.918	3.490 E-2
	4	4.054 E-4	2.147 E-15	2.136 E-4	3.615 E-7	8.918	3.490 E-2
	8	3.330 E-4	4.179 E-15	1.678 E-4	9.079 E-8	8.918	3.490 E-2
Pepper	2		–	–	–	5.738	2.233 E-2
	4	4.344 E-5	2.205 E-15	6.104 E-5	2.287 E-7	5.738	2.233 E-2
	8	7.240 E-5	4.328 E-15	1.529 E-5	5.731 E-8	5.738	2.233 E-2

Table 2. The numerical errors of images by *NSSM* with $\mu = 1$ for T, and then by *NSIM* with $\mu = 0$ for T^{-1} under perspective transformation

		T		$T^{-1}T$		True	
Items	N	$\Delta P.E.$	ΔE	$\Delta P.E.$	ΔE	$P.E.$	E
Lena	2	–	–	–	–	5.480	2.129 E-2
	4	2.317 E-4	1.442 E-6	5.035 E-4	1.869 E-6	5.479	2.129 E-2
	8	1.014 E-4	1.939 E-7	1.831 E-4	4.615 E-7	5.479	2.129 E-2
Baboon	2	–	–	–	–	11.823	4.628 E-2
	4	9.267 E-4	4.058 E-6	2.258 E-3	9.025 E-6	11.823	4.628 E-2
	8	2.317 E-4	9.780 E-7	6.561 E-4	2.201 E-6	11.823	4.628 E-2
Boots	2	–	–	–		9.200	3.600 E-2
	4	9.701 E-4	5.269 E-6	2.060 E-3	7.765 E-6	9.200	3.599 E-2
	8	2.751 E-4	7.931 E-7	5.493 E-4	1.893 E-6	9.200	3.599 E-2
Pepper	2	–	–	–	–	5.995	2.334 E-2
	4	3.330 E-4	1.382 E-6	8.850 E-4	3.384 E-6	5.995	2.334 E-2
	8	5.792 E-5	3.351 E-7	3.204 E-4	8.273 E-7	5.995	2.334 E-2

and blending models. First, consider the arbitrary geometric shape transformation T by the given boundaries in both original and distorted images. Assume $x(\xi, \eta), y(\xi, \eta) \in C^2(\Omega)$, we may define the functions $x(\xi, \eta)$ and $y(\xi, \eta)$ by the harmonic equations (see Li et al., 1989; Li, 1996):

$$\Delta x = 0, \quad \Delta y = 0, \quad (\xi, \eta) \in \Omega, \tag{76}$$

where $\Delta = \frac{\partial^2}{\partial x^2} + \frac{\partial^2}{\partial y^2}$, and the Dirichlet boundary conditions are given by:

$$x|_{\partial\Omega} = g_1(\xi, \eta), \quad y|_{\partial\Omega} = g_2(\xi, \eta). \tag{77}$$

Model is called harmonic if T: $(\xi, \eta) \to (x, y)$, where x and y satisfy (76) and (77). The harmonic model was analyzed in Li (1996) for combination CSIM of splitting–shooting-integrating methods. This study uses the NCSIM as the harmonic model, and defines the boundary as a ''heart curve:''

$$r = a(1 - \cos\theta)(a > 0), \tag{78}$$

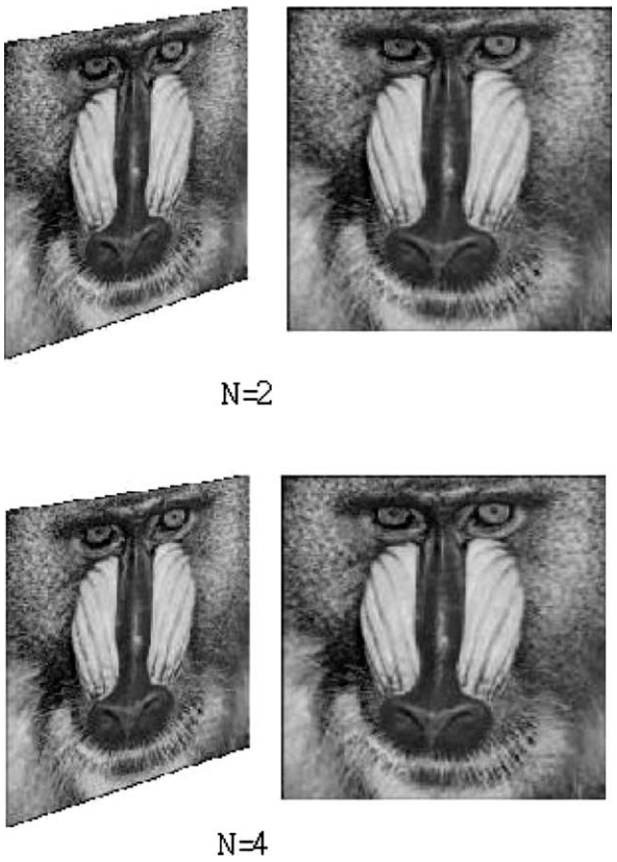

Figure 10. Baboon by *NSSM* with $\mu = 0$ for T and then by *NSIM* with $\mu = 0$ for T^{-1} under the perspective transformation.

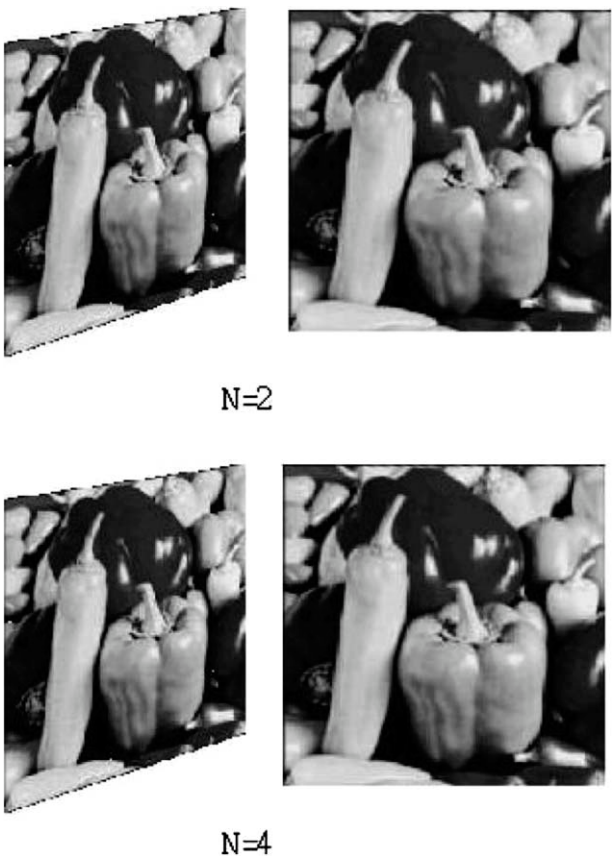

Figure 11. Pepper by *NSSM* with $\mu = 0$ for T and then by *NSIM* with $\mu = 0$ for T^{-1} under the perspective transformation.

Figure 12. Lena by *NSSM* for T and then by *NSIM* for T^{-1} under the harmonic transformation.

where a is a constant, and r is the distance from the origin to the boundary. First choose the center point as the origin of the image and then compute the angle θ in (78). Use the standard finite difference methods on the uniform grids, and choose the optimal over-relaxation iterations method to obtain the approximation solutions $\tilde{x}(\xi, \eta)$ and $\tilde{y}(\xi, \eta)$ of the harmonic transformation. As the difference solutions $\tilde{x}$ and $\tilde{y}$ can be regarded as the piecewise linear interpolation in Technique II in Section A (subsection of section III), it is easy to use the algorithms NSSM, NSIM, and NCSIM. Figure 12 shows the images tested. As the image errors are similar in magnitude to those in Tables I and II, they are omitted here. Note that the exterior edges of images in Figures 12 and 13 are quite curly. The effects of the edge curvature also produce some intensity errors, and their sequential errors may depend on N as well. Furthermore, more intensity errors come from the finite difference method for the harmonic and the biharmonic equations. In fact, Figures 12 and 13 are provided to illustrate wide applications of the algorithms of this article. To avoid confusion in verifying the error analysis made in Section IV, for Figures 12 and 13, we omit details of numerical data for the transformations.

D. Blending Transformation. Next, consider the blending model T: $(\xi, \eta) \to (x, y)$, where x and y satisfy

$$\Delta^2 x = 0, \quad \Delta^2 y = 0, \quad (\xi, \eta) \in \Omega,$$

where the biharmonic operation: $\Delta^2 = \frac{\partial^4}{\partial x^4} + 2\frac{\partial^4}{\partial x^2 \partial y^2} + \frac{\partial^4}{\partial y^4}$. The simply supported boundary conditions are given by

$$x(\xi, \eta) = g_1(\xi, \eta), \quad y(\xi, \eta) = g_2(\xi, \eta), \quad \text{on } \partial\Omega, \tag{79}$$

$$\Delta x = 0, \quad \Delta y = 0, \quad \text{on } \partial\Omega. \tag{80}$$

Alternately, the clamped supported boundary conditions are given by

$$x(\xi, \eta) = g_1(\xi, \eta), \quad y(\xi, \eta) = g_2(\xi, \eta), \quad \text{on } \partial\Omega.$$

$$\frac{\partial x}{\partial n} = 0, \quad \frac{\partial y}{\partial n} = 0, \quad \text{on } \partial\Omega,$$

where n is the outward normal of $\partial\Omega$. Split the blending model of the simply supported boundary conditions (79) and (80) into two Poisson's equations with Dirichlet conditions.

Using the numerical algorithms in this article, Figure 13 shows images under the blending model.

Remark 5.1. To close this section, let us address the numerical performance of the new algorithms NCAIM in this article. The exact integration can be achieved for the nonlinear transformation T when $N \geq N_0$, to give no sequential errors. Using the new splitting algorithms in Section III, Figures 10–13 provide images under complicated transformations. In each image, there are 256×256 $(= 65536)$ pixels with 256 intensity levels. The results of numerical and graphical experiments in Tables I and II show that by choosing small $N = 2$, there are no sequential errors numerically, and the graphical images are satisfactory for applications. Therefore, as the small N needed in the computation requires less CPU time, the proposed algorithms may also be suitable for a huge number of image transformations. Hence, the first goal of this article has been fulfilled. In contrast, many more division numbers are needed by CSIM, and

Figure 13. Boots by *NSSM* for T and then by *NSIM* for T^{-1} under the blending model of the simply supported boundary conditions.

the sequential errors always exist in ACSIM. Hence, the performance of this article is superior. Note that the splitting algorithms in this article are also applicable to the sampling process of image or picture processing in Rosenfeld and Kak (1976), Hall (1979), Russ (1992), Jähne (1997), and Ritter and Wilson (1996). Details are omitted.

VI. CONCLUDING REMARKS

To close this article, let us make a few concluding remarks.

1. This study proposes new splitting algorithms, denoted by NSSM and NSIM for images under T and T^{-1}, respectively. When the original intensity functions are chosen to be piecewise constant or piecewise linear functions, the pixel regions can be split into small triangles. The new algorithms NSSM and NSIM also avoid nonlinear solutions, and they can be applied to images with discontinuous intensity.
2. The new error analysis in Theorems 4.1, 4.2, and 4.3 yields the true errors as $O(H)$ under nonlinear transformations, where H is the pixel size. The true errors $O(H)$ are valid for both continuous and discontinuity images, even for scattered pixels. Evidently, the error analysis of image transformations in this article is much closer to the real images under transformations than our previous study of Li (1989, 1990, 1994, 1996, 1999, 1998, 2001, 2004), thus fulfilling the second goal of this article.
3. This study includes computational experiments to validate the error analysis in Section IV, and to apply the new algorithms to images under different transformations, such as perspective, harmonic, and blending transformations. Remark 5.1 shows a better performance than CSIM and ASCIM.

ACKNOWLEDGMENT

We are grateful to J. Y. Lin for the computations in Section V.

REFERENCES

E.R. Dougherty and C. R. Glardina, Image processing—continuous to discrete, geometric, transform, and statistic methods, Prentice-Hall, Englewood Cliffs, NJ, 1987; Vol. 1.

J.D. Foley, A. van Dam, S.K. Keiner, and J.K. Hughes, Computer graphics, principles and practice, Addison-Wesley Publishing, Reading, MA, 1990, p. 621.

R.C. Gonzalez and P. Wintz, Digital image processing, 2nd Ed., Addison-Wesley Publishing, Reading, MA, 1987.

Y. Gousseau and J.M. Morel, Are nature images of bounded variation? SIAM J Math Anal 33 (2002), 634–648.

E. Hall, Computer image processing and recognition, Academic Press, New York, 1979, p. 89, 215.

B. Jähne, Practical handbook on image processing for scientific applications, CRC Press, Boca Raton, New York, 1997, p. 205, 211.

Z. C. Li, Discrete techniques for computer transformations of digital images and patterns, Pattern Recognit 23 (1990), 1249–1273.

Z.C. Li, Advanced splitting-integrating methods with high convergence rates for restoring images and patterns, J Sci Comput 9 (1994), 149–172.

Z.C. Li, Analysis of discrete techniques for image transformation, Numer Algorithms 13 (1996), 225–263.

Z. C. Li, High convergence rates of digital image transformation by numerical integration using spline functions, Comput Math Appl 41 (2001), 229–251.

Z.C. Li, Advanced combinations of splitting–shooting–integrating method for digital image transformation, J Comput Appl Math 107 (1999), 147–177.

Z.C. Li and Z.D. Bai, Probabilistic analysis on the splitting–shooting method for image transformations, J Comput Appl Math 94 (1998), 69–121.

Z.C. Li, T.D. Bui, T.T. Tang, and C.Y. Suen, Computer transformations of digital images and patterns, World Scientific, Singapore, 1989.

Z.C. Li, H. Wang, and A. Liao, Numerical algorithms for image geometric Transformation and application, IEEE Trans Syst Man Cybern, Part B: Cybern 34 (2004), 132–149.

W.K. Pratt, Digital image processing, Wiley, New York, 1991.

G. X. Ritter and J. N. Wilson, Handbook of computer vision algorithms in image algebra, CRC Press, Boca Raton, New York, 1996, p. 189.

D. F. Rogers and J. A. Adams, Mathematical elements for computer graphics, McGraw-Hill Publishing Company, 1990.

A. Rosenfeld and A.C. Kak, Digital picture processing, Academic Press, New York, 1976; Chap. 4, p. 67, 68.

J. C. Russ, The image processing handbook, CRC Press, Boca Raton, FL 1992.